EFFECTS OF PROCESS PARAMETERS ON RESIDUAL STRESS AND COMPRESSIVE LAYER DEPTH DURING ULTRASONIC SURFACE ROLLING OF AA6061 ALLOY

Phan Hoang Phung, Le The Truyen*

Ho Chi Minh City University of Industry and Trade, Vietnam

*Corresponding author: truyenlt@huit.edu.vn

(Received: March 17, 2026; Revised: May 26, 2026; Accepted: June 10, 2026)

DOI: 10.31130/ud-jst.2026.24(6A).156

Abstract - This study investigates the influence of process parameters in the Ultrasonic Surface Rolling Process (USRP), including static force F_s, vibration amplitude A_0, ultrasonic frequency f, and rolling ball radius R_1, on the distribution of compressive residual stress and the depth of the compressive layer in AA6061 aluminum alloy. Based on Hertzian contact mechanics combined with an elastic–plastic mapping rule, an analytical model is developed to establish the relationship between process parameters and the characteristic outputs of the surface-hardened layer formed during USRP. The model predictions are validated through comparison with previously published experimental data. The results indicate that, within the investigated range, static force F_s has the strongest influence on both the magnitude of compressive residual stress and the depth of the compressive layer. The rolling ball radius R_1 mainly affects stress propagation into the subsurface region, whereas the vibration amplitude A_0 and ultrasonic frequency f exhibit smaller effects.

Key words - Ultrasonic surface rolling process; AA6061 aluminum alloy; Residual compressive stress; Compressive layer depth; Elasto-plastic Hertzian contact.

1. Introduction

Aluminum alloy 6061 (AA6061) is one of the important engineering materials in the Al–Mg–Si alloy system, which can be strengthened by heat treatment. It is widely used in aerospace, transportation, and precision mechanical engineering owing to its high strength-to-weight ratio, good toughness, and excellent machinability [1, 2]. However, similar to many other aluminum alloys, the surface of AA6061 usually has low hardness and is susceptible to mechanical property degradation caused by corrosion or fatigue, resulting in a reduced fatigue life of components [3, 4].

In materials mechanics, compressive residual stress (CRS) in the near-surface region is regarded as a key factor governing the fatigue resistance of components. Numerous studies have shown that CRS can delay crack initiation and slow down crack propagation, thereby improving resistance to failure under cyclic loading [3, 4].

In this context, surface strengthening based on plastic deformation has been developed to improve the surface mechanical properties of metals. Among these methods, the Ultrasonic Surface Rolling Process (USRP) is a prominent technique that combines a static force with high-frequency, low-amplitude impulses generated by an ultrasonic source. The USRP induces severe plastic deformation, leading to grain refinement, the formation of a depth-gradient structure, increased microhardness, and the generation of a CRS field with large magnitude and considerable depth in the near-surface region [5, 6]. In addition, USRP also improves the geometrical quality of the surface, contributing to an effective reduction in surface roughness [5].

The effectiveness of USRP has been confirmed for various materials. For GCr15 bearing steel, USRP produces a deep deformation layer and high CRS, significantly improving fatigue strength and microhardness compared with the untreated surface [6, 7]. Studies on 7xxx series aluminum alloys, including 7075 and 7050, have shown that CRS and the compressive layer depth strongly depend on static force, vibration amplitude, ultrasonic frequency, and rolling ball radius [8–10]. For 7050 aluminum alloy, high-speed two-dimensional ultrasonic rolling (HTUR) can form a gradient-hardened layer with a thickness of approximately 61–69 µm and generate surface compressive residual stress (CRS) of no less than −285 MPa. This beneficial CRS plays an important role in preventing the formation and propagation of fatigue cracks, thereby significantly improving the fatigue resistance of the material [10].

For AA6061, USRP has also been demonstrated to provide superior effectiveness in improving hardness, reducing roughness, and increasing CRS. Experimental results have shown that CRS can reach up to −217 MPa, while microhardness and surface quality are significantly enhanced [5, 11]. Ma et al. showed that the static force F_s has the strongest influence on the surface properties and compressive residual stress of AA6061 during USRP [5]. Meanwhile, studies on loading mechanisms have indicated that the dynamic force F_d caused by ultrasonic vibration plays an important role in the formation and depthwise distribution of residual stress [11–13].

Although USRP has been proven to significantly improve the surface mechanical properties of various metals, existing studies have mainly evaluated individual process parameters separately or focused on 7xxx series alloys. For AA6061, the combined effects of four important parameters, including static force F_s, vibration amplitude A_0, ultrasonic frequency f, and rolling ball radius R_1, on compressive residual stress (CRS) and compressive layer depth have not yet been systematically and quantitatively described. In addition, existing Hertzian contact models have mainly been developed for general materials or loading conditions and have not been calibrated according to the specific mechanical properties of AA6061, leading to limitations in quantitatively predicting surface deformation under the simultaneous action of static and dynamic loads during USRP.

Based on these limitations, this study proposes the development of a mathematical model based on Hertzian contact mechanics [14, 15] to simulate and simultaneously analyze the effects of the four process parameters on the CRS field and compressive layer depth of AA6061. The model is validated using published experimental data, thereby providing a reliable scientific basis for optimizing USRP parameters and predicting post-processing surface characteristics.

2. Analytical model based on hertzian contact for USRP

2.1. Geometrical–material setup and assumptions of the contact model

Ultrasonic surface rolling is a process that combines high-frequency ultrasonic impact energy with a static load to induce plastic deformation in the material. During ultrasonic rolling, the rolling tip remains in contact with the workpiece. Under the combined action of the static load and the impact load generated by the vibration frequency of the ultrasonic tool, the workpiece material is deformed, as illustrated in Figure 1.

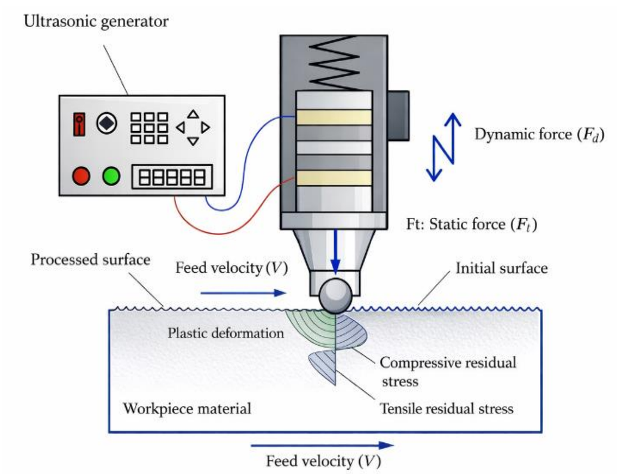

Figure 1. *Schematic illustration of the ultrasonic surface rolling process (USRP)*

Consider the elastic contact between a rolling ball with radius R_1 and the workpiece surface, which can be approximated by a convex circular arc with radius $R_2 > 0$. For the sphere–flat contact case, $R_2 \to \infty$. The materials of the two bodies, namely the ball and the workpiece, are assumed to be linearly elastic, isotropic, and subjected to small deformation. The contact is assumed to be frictionless, and the geometry is axisymmetric about the normal direction at the contact center. The z-axis is taken as positive in the direction of the applied force, with $z = 0$ located at the initial common tangent plane, while r denotes the radial coordinate, as shown in Figure 2.

Near the contact region, the unloaded surfaces of the two bodies are approximated by parabolas:

$$z_1(r) \simeq \frac{r^2}{2R_1}, z_2(r) \simeq \frac{r^2}{2R_2} \quad (1)$$

The equivalent radius of curvature and equivalent elastic modulus are defined as:

$$\frac{1}{R^*} = \frac{1}{R_1} + \frac{1}{R_2}, \ \frac{1}{E^*} = \frac{1-\nu_1^2}{E_1} + \frac{1-\nu_2^2}{E_2} \quad (2)$$

where, E_1 and ν_1 are the Young's modulus and Poisson's ratio of the rolling ball, respectively; E_2 and ν_2 are the Young's modulus and Poisson's ratio of the workpiece, respectively.

Initially, the contact between the rolling ball and the workpiece is a point contact. As the applied force increases, the contact region becomes a circular area with radius a. Under loading, within the domain $|r| \leq a$, the geometrical compatibility condition is:

$$\delta = \delta_1 + \delta_2 \quad (3)$$

$$w_1 + w_2 = \delta - (z_1 + z_2) = \delta - \frac{r^2}{2R^*} \quad (4)$$

where, δ_1 and δ_2 are the displacements of the roller and the workpiece, respectively; δ is the total displacement; and w_1 and w_2 are the normal displacements at the corresponding points on the ball and the workpiece.

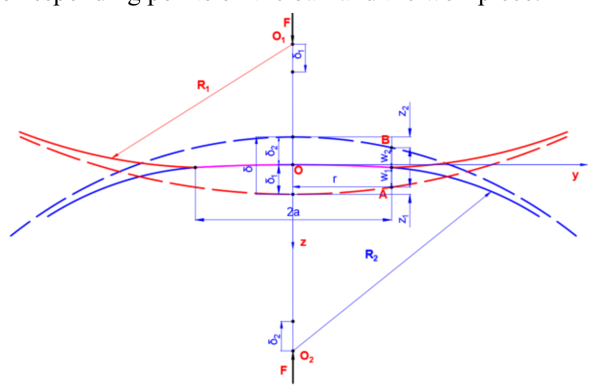

Figure 2. *Contact interaction between the rolling ball and the workpiece*

2.1.1. Static load in the ultrasonic rolling process

According to the Hertzian solution, the contact pressure is expressed as [14]:

$$p(r) = p_s\sqrt{1 - \left(\frac{r}{a_{es}}\right)^2} \quad (5)$$

Due to symmetry, the maximum pressure p_s occurs at the center $r = 0$. The static load during ultrasonic rolling is calculated as:

$$F_s = \int_0^{a_{es}} p(r) \cdot 2\pi r dr = \frac{2}{3}\pi a_{es}^2 p_s \quad (6)$$

From Eq. (6), p_s is obtained as:

$$p_s = \frac{3}{2}\frac{F_s}{\pi a_{es}^2} \quad (7)$$

For a very small contact region, the ball and the workpiece can be regarded as two elastic half-spaces. Within the domain $|r| \leq a_{es}$, the normal deflections at points A and B, denoted by w_1 and w_2, respectively, are given by the Hertzian solution [14]:

$$w_1 = \frac{(1-\nu_1^2)}{E_1}\left(\frac{\pi p_s}{4a_{es}}\right)(2a_{es}^2 - r^2) \quad (8)$$

$$w_2 = \frac{(1-\nu_2^2)}{E_2}\left(\frac{\pi p_s}{4a_{es}}\right)(2a_{es}^2 - r^2) \tag{9}$$

For a flat plate workpiece, $R_2 = \infty$. Therefore:

$$w_1 + w_2 = \delta_{es} - \frac{r^2}{2R_1} \tag{10}$$

From the equations established above, one obtains:

$$\left(\frac{(1-\nu_1^2)}{E_1} + \frac{(1-\nu_2^2)}{E_2}\right)\left(\frac{\pi p_s}{4a_{es}}\right)(2a_{es}^2 - r^2) = \delta_{es} - \frac{r^2}{2R_1} \tag{11}$$

Using the definition of the equivalent elastic modulus E^*, we have:

$$\left(\frac{\pi p_s}{4a_{es}E^*}\right)(2a_{es}^2 - r^2) = \delta_{es} - \frac{r^2}{2R_1} \tag{12}$$

At r = 0:

$$\delta_{es} = \frac{\pi p_s a_{es}}{2E^*} \tag{13}$$

At r = a_{es}:

$$a_{es} = \frac{\pi p_s R_1}{2E^*} \tag{14}$$

Substituting the above expressions into Eqs. (13) and (14), the expressions for the contact radius a_{es}, indentation depth δ_{es}, and maximum pressure p_s are obtained as follows:

$$a_{es} = \left(\frac{3F_s R_1}{4E^*}\right)^{\frac{1}{3}} \tag{15}$$

$$\delta_{es} = \left(\frac{9{F_s}^2}{16{E^*}^2 R_1}\right)^{\frac{1}{3}} \tag{16}$$

$$p_s = \left(\frac{6F_s{E^*}^2}{\pi^3{R_1}^2}\right)^{\frac{1}{3}} \tag{17}$$

From the above expressions, we obtain:

$$a_{es} = \sqrt{R_1\delta_{es}} \tag{18}$$

$$F_s = \frac{4}{3}E^* R_1^{1/2}{\delta_{es}}^{3/2} \tag{19}$$

2.1.2. Dynamic load in the ultrasonic rolling process

In addition to the static load, during ultrasonic rolling, the rolling tip undergoes high-frequency harmonic vibration, thereby generating a cyclic dynamic load acting on the surface of the AA6061 workpiece. The vibrational displacement of the rolling tip along the direction of the applied force is described by the harmonic function:

$$x(t) = A_0\sin(2\pi f t) \tag{20}$$

where A_0 is the ultrasonic vibration amplitude and f is the vibration frequency.

The instantaneous velocity of the rolling tip is determined by differentiating the displacement with respect to time:

$$v(t) = \frac{dx}{dt} = 2\pi f A_0\cos(2\pi f t) \tag{21}$$

Therefore, the maximum velocity of the rolling tip within one vibration cycle is:

$$v_{max} = 2\pi f A_0 \tag{22}$$

When the rolling tip impacts the workpiece surface, the kinetic energy of the rolling tip at the instant of impact is converted into elastic deformation work in the contact region. This process is described based on the principle of energy conservation:

$$\frac{1}{2}mv_{max}^2 = \int_0^{\delta_{ed}} F_d(\delta)\,d\delta \tag{23}$$

Where $m = \frac{4}{3}\pi R_1^3\rho$ is the mass of the rolling tip, and ρ is the density of the rolling ball material. The equivalent dynamic contact force is indirectly derived through the elastic indentation caused by impact, based on the principle of energy conservation:

$$F_d(\delta) = \frac{4}{3}E^* R_1^{1/2}{\delta_{ed}}^{3/2} \tag{24}$$

Substituting the above expression into Eq. (23) gives:

$$\frac{1}{2}mv_{max}^2 = \int_0^{\delta_{ed}}\left(\frac{4}{3}E^* R_1^{1/2}\delta^{3/2}\right)d\delta \tag{25}$$

Solving the integral and substituting the maximum velocity from Eq. (22), the elastic indentation caused by the dynamic load is determined as:

$$\delta_{ed} = \left(\frac{5\rho\pi^3 R_1^{5/2} f^2 A_0^2}{E^*}\right)^{2/5} \tag{26}$$

According to the geometrical relationship of Hertzian contact, the elastic contact radius caused by the dynamic load is determined as:

$$a_{ed} = \sqrt{R_1\delta_{ed}} \tag{27}$$

The maximum compressive pressure caused by the dynamic load is determined in a manner similar to the static loading case, based on the dynamic contact radius:

$$p_d = \frac{2E^*}{\pi R_1}a_{ed} \tag{28}$$

2.1.3. Effective contact model under the simultaneous action of static and dynamic loads

In this study, the simultaneous effects of the static force and ultrasonic vibration are represented by an equivalent effective contact state. Accordingly, the static and dynamic loads are considered separately to determine the contact characteristics based on Hertzian theory, including the contact radius and characteristic contact pressure. These quantities are then combined to construct an overall contact state used for residual stress field analysis.

The effective elastic contact radius is determined as:

$$a_e = a_{es} + a_{ed} \tag{29}$$

Similarly, the equivalent maximum contact pressure on the workpiece surface is determined as:

$$p_0 = p_s + p_d \tag{30}$$

It should be noted that the relations in Eqs. (29) and (30) do not represent the direct summation of static and dynamic loads over time. Instead, they provide an approximate description based on an effective average contact state, intended to reflect the cumulative influence of successive ultrasonic loading cycles on the contact region.

This assumption is established on the basis that the ultrasonic vibration frequency is much higher than the characteristic deformation rate of the material, while plastic deformation accumulates gradually over the processing time. Therefore, the cyclic dynamic load can be approximately converted into an equivalent impact force based on the effective average value of the loading cycle.

This approach is consistent with previously published analytical models in USRP studies [11, 13], in which the ultrasonic dynamic load is converted into an equivalent contact impact force and combined with the static load. As a result, the model can describe the influence trends of process parameters on material behavior.

2.2. Hertzian contact relationship and elastic stress field along the depth direction

In the USRP model, the contact region between the spherical ball and the workpiece is modeled according to Hertzian theory as a circular contact area with radius a_e. The contact pressure follows a semi-elliptical distribution: $p(r) = p_0\sqrt{1-\left(\frac{r}{a_e}\right)^2}$ với $0 \le r \le a_e$. The quantities a_e and p_0 are determined from Eqs. (29) and (30). In an axisymmetric coordinate system passing through the contact center, the Hertzian solution for the elastic stress field along the z-axis is given by [14]:

$$\sigma_x^e = \sigma_y^e = p_0\left[\frac{1}{2}\ A(\xi) - (1+\nu_2)B(\xi)\right] \quad (31)$$

$$\sigma_z^e = -p_0 A(\xi) \quad (32)$$

Where $\xi = \frac{z}{a_e}$ and the scalar functions are:

$$A(\xi) = \frac{1}{1+\xi^2}, B(\xi) = 1 - \xi \arctan\left(\frac{1}{\xi}\right) \quad (33)$$

In a form convenient for numerical calculation, by substituting $\xi = \frac{z}{a_e}$, we have:

$$\sigma_x^e = \sigma_y^e$$

$$\sigma_x^e = p_0\left[\frac{1}{2}\frac{1}{1+\left(\frac{z}{a_e}\right)^2} - (1+\nu_2)\left(1 - \frac{z}{a_e}\arctan\left(\frac{a_e}{z}\right)\right)\right] \quad (34)$$

$$\sigma_z^e = -\frac{p_0}{1+(z/a_e)^2} \quad (35)$$

From Eqs. (31)–(35), the von Mises equivalent stress is determined by:

$$\sigma_i^e = \sqrt{\frac{1}{2}\left[\left(\sigma_x^e-\sigma_y^e\right)^2 + \left(\sigma_y^e-\sigma_z^e\right)^2 + (\sigma_z^e-\sigma_x^e)^2\right]} \quad (36)$$

For the axisymmetric problem, where $\left(\sigma_x^e = \sigma_y^e\right)$, Eq. (36) is simplified as: $\sigma_i^e = |\sigma_x^e - \sigma_z^e|$

The elastic strains are obtained from the generalized Hooke's law for isotropic materials [15, 16]:

$$\varepsilon_x^e = \frac{1}{E_2}\left[\sigma_x^e - \nu_2\left(\sigma_y^e + \sigma_z^e\right)\right],$$
$$\varepsilon_y^e = \frac{1}{E_2}\left[\sigma_y^e - \nu_2(\sigma_x^e + \sigma_z^e)\right], \quad (37)$$
$$\varepsilon_z^e = \frac{1}{E_2}\left[\sigma_z^e - \nu_2\left(\sigma_x^e + \sigma_y^e\right)\right]$$

The conventional equivalent strain, proportional to the von Mises stress, is:

$$\varepsilon_i^e = \frac{\sigma_i^e}{E_2} \quad (38)$$

For mechanical analysis, the hydrostatic and deviatoric components are separated. The hydrostatic components of stress and strain are:

$$\sigma_m^e = \frac{1}{3}\left(\sigma_x^e + \sigma_y^e + \sigma_z^e\right), \varepsilon_m^e = \frac{1}{3}\left(\varepsilon_x^e + \varepsilon_y^e + \varepsilon_z^e\right) \quad (39)$$

The deviatoric stresses are:

$$S_x^e = \sigma_x^e - \sigma_m^e, S_y^e = \sigma_y^e - \sigma_m^e, S_z^e = \sigma_z^e - \sigma_m^e \quad (40)$$

Along the axis of symmetry, from Eqs. (39) and (40), one obtains:

$$S_x^e = S_y^e = \frac{1}{3}\sigma_i \text{ and } S_z^e = -\frac{2}{3}\sigma_i \quad (41)$$

For linear isotropic elasticity:

$$e_{ij}^e = \frac{S_{ij}^e}{2G}, G = \frac{E_2}{2(1+\nu_2)} \text{ [15, 16]}$$

Accordingly, the deviatoric strains expressed in terms of stress components are:

$$e_x^e = e_y^e = \frac{1}{3}(1+\nu_2)\,\varepsilon_i^e, e_z^e = -2\,e_x^e \quad (42)$$

2.3. Stress–strain analysis in plastic contact

Model assumptions are as follows: the rolling tip is regarded as perfectly rigid, while the AA6061 workpiece is considered an isotropic elastic–plastic material. When the stress at a point reaches the yield threshold σ_s, the material enters the plastic yielding state, and the plastic region expands with the applied load level. To ensure feasibility and efficiency when investigating parameters over a wide domain, instead of directly solving the full nonlinear elastic–plastic contact problem, this study adopts the elastic-to-plastic mapping rule proposed by Li et al. [17]. This approach enables the elastic contact state obtained from the Hertzian solution to be transformed into an equivalent elastic–plastic state at low computational cost. It has also been used in previous studies on residual stress modeling induced by surface deformation treatments [11, 13, 17]. The mapping rule is expressed by Eqs. (43)–(44), combined with the plastic stress–strain relationship in Eq. (61) and the plastic deviatoric stress tensor in Eqs. (62)–(66).

At each point at depth $z$from the surface, let ε_i^e denote the equivalent elastic strain derived from the Hertzian field in Section 2.2, ε_i^p denote the equivalent plastic strain to be determined, and $\varepsilon_s$denote the strain at the yield threshold corresponding to σ_s. The transformation rule is written as follows:

$$\varepsilon_i^p = \begin{cases} \varepsilon_i^e, \ \varepsilon_i^e \le \varepsilon_s \\ \varepsilon_s + \alpha(\varepsilon_i^e - \varepsilon_s), \ \varepsilon_i^e > \varepsilon_s \end{cases} \quad (43)$$

where α is determined from the ratio between the overall plastic contact radius and the effective elastic contact radius:

$$\alpha = \frac{a_p}{a_e} \quad (44)$$

Here, a_e is the overall elastic contact radius determined in Eq. (29), while a_p is the plastic contact radius derived below. The coefficient α reflects the degree of expansion of the plastic deformation region relative to the elastic contact region, thereby characterizing the tendency of AA6061 to yield under the applied loading during USRP. The pair of Eqs. (43)–(44) allows the plastic strain field to be directly inferred from the elastic field without solving the full nonlinear plasticity problem. The present model inherits the theoretical basis of Li et al. [17] and is extended to the combined static–dynamic loading condition of the USRP process. The model is not separately calibrated using experimental data for AA6061; instead, material characteristics are considered through input mechanical parameters such as elastic modulus, Poisson's ratio, yield strength, and the hardening law.

2.3.1. Static load

The plastic contact radius a_p is determined as follows. Let F_s be the applied compressive force. According to the work–energy principle:

$$\int_0^{\delta_{sp}} F_s \, d\delta = \int_0^{\delta_{sp}} \bar{p} \, S(\delta) \, d\delta \tag{45}$$

where $\bar{p}$ is the mean pressure in the plastic contact region, assumed to be constant and taken as $\bar{p} = 3\sigma_s$ [14, 17], and σ_s is the yield strength of the workpiece material. The contact area Sdepends on the geometry of the plastic indentation.

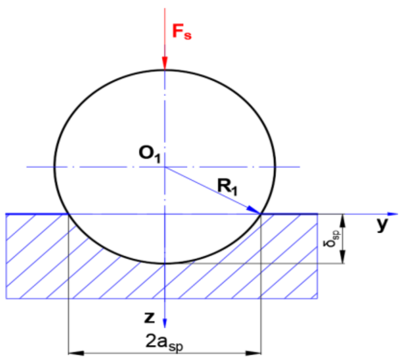

Figure 3. *Geometrical model of the plastic indentation zone*

The geometry of the plastic indentation region is given by:

$$R_1^2 = \left(R_1 - \delta_{sp}\right)^2 + a_{sp}^2 \tag{46}$$

Assuming that the contact region is very small, $\delta_{sp} \ll R_1$, we have:

$$a_{sp} = \sqrt{2R_1 \, \delta_{sp}} \tag{47}$$

The contact area as a function of δ_{sp} is:

$$S\left(\delta_{sp}\right) = \pi a_{sp}^2 \approx 2\pi R_1 \, \delta_{sp} \tag{48}$$

Substituting Eq. (48) into Eq. (45), and assuming that F_s remains constant during the increase in δ_{sp}, yields:

$$F_s \, \delta_{sp} = \int_0^{\delta_{sp}} \bar{p} \, (2\pi R_1 \, \delta) \, d\delta = \bar{p} \, \pi R_1 \, \delta_{sp}^2$$
$$\Rightarrow \delta_{sp} = \frac{F_s}{\bar{p} \, \pi R_1} = \frac{F_s}{3\pi R_1 \, \sigma_s} \tag{49}$$

From Eqs. (47)–(49), it follows that:

$$a_{sp} = \sqrt{2R_1 \, \delta_{sp}} = \sqrt{\frac{2F_s}{3\pi \, \sigma_s}} \tag{50}$$

2.3.2. Dynamic load

During ultrasonic rolling, in addition to local plastic deformation caused by the static load, the ultrasonic vibration of the rolling ball also produces short-duration dynamic impacts at high velocity, resulting in the formation of an additional plastic deformation region caused by the dynamic load. The geometrical characteristics of the plastic indentation region generated by dynamic impact are determined based on dynamic equilibrium and the assumption of fully plastic contact.

According to Newton's second law, the inertial force of the ball during impact is balanced by the mean deformation-resisting pressure acting over the plastic contact area:

$$\frac{4}{3} \pi \rho R_1^3 \frac{dv}{dt} = \bar{p} \, A_{dp} = \bar{p} \, \pi a_{dp}^2 \tag{51}$$

Let δ_{dp} be the plastic indentation caused by the dynamic load. The kinematic relation is:

$$v = \frac{d\delta_{dp}}{dt} \tag{52}$$

Therefore, the dynamic equilibrium equation can be rewritten as:

$$\frac{4}{3} \pi \rho R_1^3 \, v \, dv = \bar{p} \, \pi a_{dp}^2 \, d\delta_{dp} \tag{53}$$

According to the geometrical relation of sphere–flat contact in the small-deformation regime, the plastic contact radius caused by the dynamic load is determined as:

$$a_{dp} = \sqrt{2R_1 \delta_{dp}} \tag{54}$$

Substituting Eq. (54) into Eq. (53) and integrating with respect to δ_{dp} gives:

$$\frac{3}{2} \pi \rho R_1^2 \, v^2 = \bar{p} \, \delta_{dp}^2 \tag{55}$$

Thus, the plastic indentation caused by the dynamic load is:

$$\delta_{dp} = \sqrt{\frac{2 \, \rho \, R_1^2 \, v^2}{9 \, \sigma_s}} \tag{56}$$

During ultrasonic rolling, the maximum impact velocity of the rolling ball is determined by ultrasonic vibration:

$$v_{max} = 2\pi A_0 f \tag{57}$$

Substituting $v = v_{\max}$into Eq. (56), the maximum plastic indentation caused by the dynamic load is determined as:

$$\delta_{dp} = \pi R_1 A_0 f \sqrt{\frac{8 \, \rho}{9 \, \sigma_s}} \tag{58}$$

From the geometrical relation in Eq. (54), the plastic deformation radius caused by the dynamic load is determined as:

$$a_{dp} = R_1 \left(\frac{32 \, \rho \, \pi^2 \, A_0^2 \, f^2}{9 \, \sigma_s}\right)^{1/4} \tag{59}$$

During ultrasonic rolling, the total plastic deformation region is assumed to be formed by the superposition of the plastic regions generated by the static and dynamic loads. Therefore, the total plastic deformation radius is determined as:

$$a_p = a_{sp} + a_{dp} \tag{60}$$

The equivalent plastic stress can be calculated from the elastic–plastic stress-strain curve [13] as follows:

$$\sigma_i^p = \begin{cases} \sigma_i^e \\ \sigma_s + H_1(\varepsilon_i^p - \varepsilon_s) \\ \sigma_b + H_2(\varepsilon_i^p - \varepsilon_b) \end{cases} \begin{cases} \varepsilon_i^p < \varepsilon_s \\ \varepsilon_s \le \varepsilon_i^p < \varepsilon_b \\ \varepsilon_i^p \ge \varepsilon_b \end{cases} \tag{61}$$

where: $H_1 = (\sigma_b - \sigma_s)/(\varepsilon_b - \varepsilon_s)$, $\varepsilon_s = \sigma_s / E_2$. Here, σ_b is the ultimate tensile stress of the ultrasonically rolled body, and ε_b is the strain corresponding to σ_b; H_1 and H_2 are linear hardening coefficients in different stress–strain regions. In this study, the case without additional hardening beyond ε_b is considered; therefore, $H_2 = 0$. Accordingly, the segment $\varepsilon_i^p \ge \varepsilon_b$ becomes $\sigma_i^p = \sigma_b$.

In the isotropic elastic–plastic model, the stress field is decomposed into hydrostatic and deviatoric components. The hydrostatic component only causes volumetric change and does not activate yielding, whereas the deviatoric component governs the development of plastic deformation. For the axisymmetric configuration described in Section 2.3, the formal invariance of the relationship between strain and stress tensors is assumed to extend from the elastic domain to the elastic–plastic domain. Under this assumption, the plastic deviatoric strain e_{ij}^p can be expressed compactly in terms of the equivalent plastic strain ε_i^p:

$$e_x^p = e_y^p = \frac{1}{3}(1+\nu_2)\varepsilon_i^p \tag{62}$$

$$e_z^p = -\frac{2}{3}(1+\nu_2)\varepsilon_i^p \tag{63}$$

Based on the expression of the deviatoric tensor in Iliushin's elastic–plastic theory, the plastic deviatoric stress is related to the plastic deviatoric strain through the effective plastic modulus in the equivalent direction [9]:

$$S_{ij}^p = \frac{1}{(1+\nu_2)}\frac{\sigma_i^p}{\varepsilon_i^p}e_{ij}^p \tag{64}$$

Substituting Eqs. (62)–(63) into Eq. (64), the plastic deviatoric stress tensor is obtained as:

$$S_x^p = S_y^p = \frac{1}{3}\sigma_i^p, \tag{65}$$

$$S_z^p = -\frac{2}{3}\sigma_i^p = -2S_x^p \tag{66}$$

2.4. Residual stress after unloading

In the calculation of residual stress, the model adopts standard assumptions of elastic–plastic mechanics: (i) AA6061 is considered isotropic with an isotropic hardening mechanism, and the Bauschinger effect is neglected; (ii) the deformation induced by USRP lies within the small-to-moderate deformation range, and unloading follows an elastic law until reverse yielding occurs; (iii) plastic yielding follows the von Mises criterion, in which the hydrostatic stress component does not govern yielding, whereas the deviatoric component plays the dominant role [11, 13]. Under these assumptions, the initial residual stress immediately after unloading is determined as:

$$\sigma_{ij}^r = s_{ij}^{p*} - s_{ij}^e \tag{67}$$

where s_{ij}^{p*} is the plastic deviatoric stress tensor at the onset of unloading, and s_{ij}^e is the corresponding elastic deviatoric stress tensor. Based on the relationship between σ_i^e and the yield threshold σ_s, the unloading process is divided into three regions as follows.

Region A — Completely elastic unloading, ($\sigma_i^e < \sigma_s$) At the point considered, the material has not previously yielded. After unloading:

$$\sigma_{ij}^r = 0 \tag{68}$$

Region B — Unloading without reverse yielding ($\sigma_s \le \sigma_i^e < 2\sigma_i^p$)

From the condition that the deviatoric tensor has a zero sum in the three principal directions, one obtains:

$$\sigma_x^r = \sigma_y^r = \frac{1}{3}\left(\sigma_i^p - \sigma_i^e\right) \tag{69}$$

$$\sigma_z^r = -\frac{2}{3}\left(\sigma_i^p - \sigma_i^e\right) \tag{70}$$

Region C — Reverse yielding and hardening during unloading ($\sigma_i^e > 2\sigma_i^p$)

If $\sigma_i^e > 2\sigma_i^p$, reverse yielding accompanied by hardening occurs in the material. First, the stress level $2\sigma_i^p$ is elastically unloaded; then, the remaining stress component:

$$\Delta\sigma_i^e = \sigma_i^e - 2\,\sigma_i^p \tag{71}$$

continues to cause reverse yielding during unloading. The corresponding elastic strain is:

$$\Delta\varepsilon_i^e = \frac{\Delta\sigma_i^e}{E_2} \tag{72}$$

and the plastic strain is assumed to be proportional to it:

$$\Delta\varepsilon_i^p = \alpha\,\Delta\varepsilon_i^e \tag{73}$$

The increase in yield stress due to hardening is determined as:

$$\Delta\sigma_i^p = H_1\,\Delta\varepsilon_i^p \tag{74}$$

Accordingly, the residual stresses in the x, y, and z directions are written as:

$$\sigma_x^r = \sigma_y^r = -\frac{1}{3}\left(\sigma_i^p + \Delta\sigma_i^p\right) \tag{75}$$

$$\sigma_z^r = -2\,\sigma_x^r \tag{76}$$

During USRP, each rolling–impact cycle of the ultrasonic ball generates a residual stress field after unloading, denoted by σ_{ij}^r. When 100% coverage is achieved with sufficient overlap, the deformation field approaches a stable and continuous state along the rolling track. The deformation of the surface layer can be regarded as homogeneous in the plane, independent of x and y, and dependent only on the depth z. In this case, the final residual stress field satisfies:

$$\sigma_x = \sigma_y = f_1(z), \sigma_z = 0 \tag{77}$$

To transform the transient field σ_{ij}^r into the final state, the temporary normal component is eliminated while keeping the in-plane strain unchanged:

$$\Delta\varepsilon_x = \Delta\varepsilon_y = 0, \Delta\sigma_z = -\,\sigma_z^r \tag{78}$$

According to the incremental form of Hooke's law for isotropic elastic materials with E_2 and ν_2, the compensating in-plane stress caused by the Poisson effect is determined as:

$$\sigma_x^{\text{rel}} = \sigma_y^{\text{rel}} = \left(\frac{\nu_2}{1-\nu_2}\right)\sigma_z^r \tag{79}$$

Therefore, the final residual stress field is:

$$\sigma_x^R = \sigma_y^R = \sigma_x^r - \sigma_x^{\text{rel}} = \frac{1+\nu_2}{1-\nu_2}\,\sigma_x^r \tag{80}$$

$$\sigma_z^R = 0 \tag{81}$$

2.5. Applicable limits of the model

The present analytical model is developed based on Hertzian contact, homogeneous isotropic material behavior, small-to-moderate deformation, and frictionless contact conditions. Therefore, the model is suitable for single-pass processing and for analyzing the influence trends of process parameters within the investigated range of this study.

In this model, the rolling ball is assumed to be perfectly rigid because the elastic modulus of the WC–Co material is significantly higher than that of AA6061; thus, most deformation occurs in the workpiece. The assumption of isotropic hardening is used to describe the increase in yield strength with accumulated plastic strain. The unloading process is described using an approximate elastic–plastic scheme to represent stress recovery after load removal.

For cases involving large applied forces, severe plastic deformation, multiple successive rolling passes, thermal effects, or cyclic-load-dependent material behavior, the accuracy of the model may decrease. In addition, the present model does not consider the Bauschinger effect and therefore cannot fully reflect the material response under load reversal in the localized cyclic loading conditions of USRP. In such cases, nonlinear numerical models such as the finite element method may provide a more appropriate approach.

3. Simulation and computational method

The simulation model was developed based on the Hertzian contact equation system and the elastic–plastic model presented in Section 2. The entire computational procedure in this study was implemented using MATLAB. The program was developed to automatically perform the calculation steps of the model, including determination of the Hertzian contact state, stress–strain field along the depth direction, elastic–plastic mapping, unloading simulation, and derivation of the residual stress distribution. The results were used to determine the surface residual stress and the compressive layer depth according to the criteria in Eqs. (83)–(84). In all computational steps, the WC–Co ball tip was regarded as perfectly rigid, whereas the AA6061-T6 workpiece was modeled as an isotropic elastic–plastic material, with linear elasticity up to the yield limit and linear hardening characterized by the tangent modulus H_1. The material parameters were collected from previously published experimental studies on AA6061 and WC–Co [5, 6, 11].

The total contact force in each USRP cycle consists of the static force F_s and the dynamic force F_d. The dynamic force F_d originates from the harmonic vibration of the vibration system at frequency f and amplitude A_0. To properly reflect the dynamic characteristics of the rolling ball, the effective mass of the vibration system was calculated according to the geometry of the ball:

$$m_1 = \rho_1 \cdot \frac{4}{3}\pi R_1^3 \tag{82}$$

where ρ_1 is the density of the WC–Co material, as listed in Table 1. This ensures that m_1 varies with the rolling ball radius R_1, which is consistent with practical conditions and fully agrees with the dynamic loading model presented in Section 2.2.

Hertzian contact quantities, such as the contact radius a_e, indentation depth δ, and maximum pressure p_0, were calculated directly from Eqs. (15)–(17). The elastic stress–strain field along the depth direction was determined from the Hertzian solution according to Eqs. (31)–(39).

To describe plastic behavior without solving the full nonlinear elastic–plastic contact problem, the simulation employed the elastic–plastic mapping rule of Li et al., given by Eqs. (43)–(44). This rule enables the equivalent plastic strain to be derived from the equivalent elastic strain through a correction coefficient α, which is proportional to the degree of yield-threshold exceedance. The equivalent plastic stress was calculated according to the hardening curve in Eq. (61), and the plastic deviatoric stress tensor was determined using Eqs. (62)–(66).

The unloading process was divided into three behavioral regions, as described in Eqs. (68)–(74): completely elastic unloading, unloading without reverse yielding, and unloading with reverse yielding accompanied by hardening. The final residual stress field was determined from Eqs. (80) and (81), considering the plane-strain condition corresponding to continuous USRP treatment on the surface.

The subsurface domain was discretized using a one-dimensional (1D) mesh over the range $0 \leq z \leq 4$ mm with a step size of $\Delta z = 1\mu\text{m}$, allowing accurate evaluation of the evolution of residual stress along the depth direction.

Two output indicators were determined:

- Surface residual stress: $\sigma_x^R\ (0^+)$ (83)
- Compressive layer depth:

$$d_c = \max\ \{z \geq 0 \mid \sigma_x^R(z) < 0\} \tag{84}$$

Table 1. *Mechanical properties of materials used in the USRP simulation*

Material	Density ρ (kg/m³)	Young's modulus E (Pa)	Poisson's ratio ν	Yield strength σs (Pa)
AA6061-T6	2.75×10^3	5.22×10^{10}	0.33	1.5×10^8
WC–Co (ball)	1.563×10^4	7.10×10^{11}	0.31	Assumed rigid body

Note: *The data for AA6061-T6 are taken from [5,11]; the data for WC–Co are taken from [6].*

To investigate the influence of process parameters on residual stress and compressive layer depth during USRP, this study established a set of 12 simulation configurations using a near-orthogonal design method. This design was intended to cover the investigated parameter domain with a reasonable number of computational cases. The four selected input parameters were static force F_s, vibration amplitude A_0, ultrasonic frequency f, and rolling ball radius R_1.

The investigated levels were determined based on previous experimental and modeling studies on USRP for AA6061 aluminum alloy and similar materials [1, 11–13]. They also fall within the parameter range commonly used in practice, ensuring stable contact and avoiding excessive deformation. The corresponding simulation configurations are presented in Table 2.

The configurations in Table 2 were used to construct the simulation dataset within the investigated parameter domain. In addition, to clarify the influence trend of each parameter on the residual stress distribution along the depth direction, the results in Section 4 are presented using a one-factor-at-a-time method, in which the other three parameters are kept fixed at their reference values.

Table 2. *Simulation configurations based on the near-orthogonal design*

Configuration	Fs (N)	A0 (μm)	f (kHz)	R1 (mm)
1	100	3	20	4
2	100	4	25	5
3	100	5	30	6
4	200	3	25	6
5	200	4	30	4
6	200	5	20	5
7	300	3	30	5
8	300	4	20	6
9	300	5	25	4
10	150	3	20	5
11	250	4	25	6
12	350	5	30	4

4. Results and discussion

The depthwise distribution of residual stress $\boldsymbol{\sigma_x^R(z)}$ during ultrasonic surface rolling exhibits a characteristic pattern: the compressive stress increases in absolute magnitude, reaches the maximum compressive value at a subsurface position, and then gradually decreases toward zero. In this study, the magnitude of compressive stress is considered in terms of its absolute value, while the negative sign only indicates the compressive nature of the stress.

4.1. Effect of static force F_s

The investigated conditions were: $A_0 = 3\mu\text{m}$, $f = 20\text{kHz}$, $R_1 = 4\text{mm}$, and $F_s \in \{100,200,300\}\text{N}$.

From Figure 4(a), as the static force F_s increases:

- The compressive stress in the near-surface region increases markedly, as reflected by the increase in the maximum compressive value in terms of absolute magnitude.
- At the same depth, the difference among the curves is large throughout the investigated domain, indicating that F_s significantly changes the stress value over the entire depth range.
- The position where $\sigma_x^R(z) = 0$, namely d_c, shifts deeper into the material, indicating a change in the compressive layer depth within the plotted range.

Thus, in the investigated cases, $F_s$simultaneously changes both the compressive stress value and the position of the compressive layer depth, and this difference is clearly reflected over the entire depth domain of the curves. This trend is consistent with previously published experimental and theoretical results for AA6061 after USRP [11].

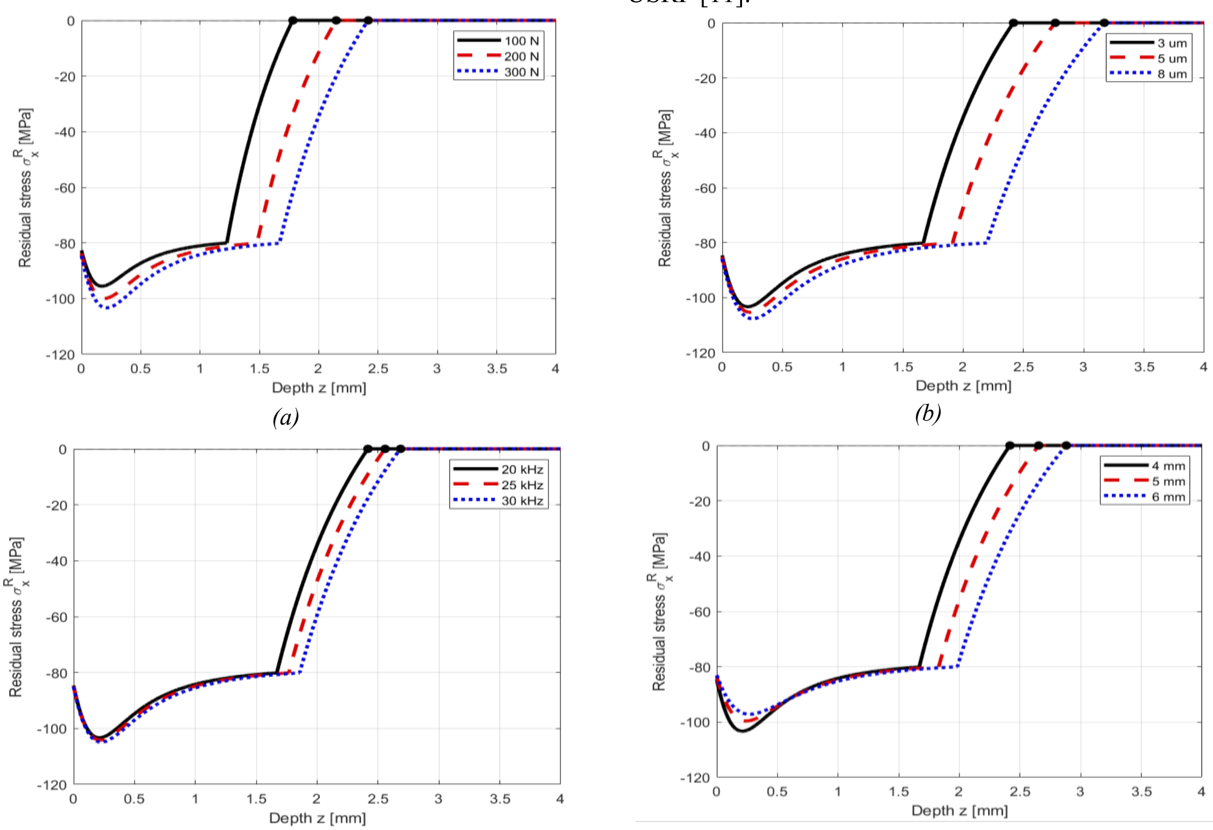

(a) *(b)* *(c)* *(d)*

Figure 4. *Influence of ultrasonic surface rolling parameters on residual stress and compressive layer depth: (a) static load, (b) ultrasonic amplitude, (c) ultrasonic frequency, and (d) ball radius*

4.2. Effect of ultrasonic vibration amplitude A_0

The investigated conditions were: $F_s = 300\text{N}$, $f = 20\text{kHz}$, $R_1 = 4\text{mm}$, and $A_0 \in \{3,5,8\}\mu\text{m}$.

From Figure 4(b), as the vibration amplitude A_0 increases:

- The compressive stress in the near-surface region increases, as indicated by the increase in the maximum compressive value in terms of absolute magnitude.

• At the same depth, the difference among the curves is smaller than that observed for F_s, especially in the intermediate region.

• The position where $\sigma_x^R(z) = 0$, namely d_c, shifts deeper, showing that the compressive layer depth varies with A_0.

A notable feature is that the curves tend to shift in a relatively similar manner, indicating that A_0 mainly changes the level of compressive stress, whereas the depthwise differentiation among the cases is not substantial.

4.3. *Effect of ultrasonic frequency f*

The investigated conditions were: $F_s = 300$N, $A_0 = 3$μm, $R_1 = 4$mm, and $f \in \{20,25,30\}$kHz.

From Figure 4(c), as the ultrasonic frequency f increases:

• The compressive stress increases slightly over the entire depth domain, as reflected by the downward shift of the $\sigma_x^R(z)$ curves.

• The difference among the curves at the same depth is small, indicating that the influence of f on the stress value is limited within the investigated range.

• The position where $\sigma_x^R(z) = 0$, namely d_c, changes, but the shift is small.

Thus, among the investigated parameters, f mainly affects the compressive stress level, while its effects on the compressive layer depth and depthwise distribution are not pronounced from the graphical results. This trend is consistent with theoretical–experimental studies on residual stress fields in USRP when considering the role of the dynamic loading component [11–13].

4.4. *Effect of rolling ball radius* R_1

The investigated conditions were: $F_s = 300$N, $A_0 = 3$μm, $f = 20$kHz, and $R_1 \in \{4,5,6\}$mm.

Figure 4(d) shows that the rolling ball radius R_1 has a clear influence on the depthwise distribution of residual stress.

Specifically:

• As increases, the maximum compressive value in the near-surface region decreases in terms of absolute magnitude, indicating a weaker surface compression level.

• In the intermediate region, the curves tend to be closer to each other, showing that the influence of R_1 is smaller than that in the near-surface region.

• In the deeper region, the position where the stress returns to zero shifts further into the material as R_1 increases, meaning that the compressive layer depth d_c increases with R_1.

This result is consistent with the Hertzian contact mechanism, in which the contact radius increases with R_1, reducing the maximum contact pressure while simultaneously expanding the loaded region, thereby influencing the stress distribution along the depth direction [8–10].

4.5. Model reliability evaluation through experimental comparison

Figure 5 presents a comparison of the depthwise residual stress distribution $\sigma_x^R(z)$between the simulation results and the experimental data of Ma et al. [1]. The process conditions used in the simulation were selected to correspond to the referenced experimental case, including static force $F_s = 300$N, ultrasonic frequency $f = 20$kHz, vibration amplitude $A_0 = 3$μm, and rolling ball radius $R_1 = 4$mm.

Overall, the two curves show good similarity in the morphology of the residual stress distribution along the depth direction. Both the simulation and the experiment indicate that the compressive residual stress increases in absolute magnitude from the surface to a subsurface position, where it reaches the maximum compressive value, corresponding to the minimum value under the negative sign convention, and then gradually decreases and approaches zero with increasing depth into the material.

Quantitative evaluation shows that in the near-surface region, at approximately $z \approx 0$ mm, the residual stress predicted by the model reaches about −86 MPa, whereas the experimental value is approximately −85 MPa, corresponding to a relative error of about 1.2%. The maximum compressive value predicted by the model reaches approximately −110 MPa at $z \approx 0.20$ mm, while the experimental result reaches approximately −107 MPa at $z \approx 0.18$ mm. The error in magnitude is about 2.8%, while the error in the position of the maximum compressive value is approximately 11.1%.

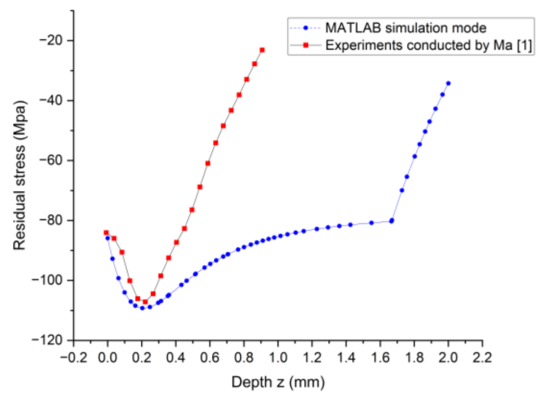

Figure 5. *Comparison of residual stress depth profiles between the proposed model and the experimental data of Ma et al. [1]*

At greater depths, the discrepancy between the simulation and experiment increases markedly. The experimental results show that the compressive residual stress decreases rapidly and approaches zero at approximately $z \approx 1.0$ mm, whereas the model still maintains a compressive state up to approximately $z \approx 2.0$ mm.

The discrepancy mainly arises from the idealized assumptions of the model. The ultrasonic load is converted into an equivalent average effective contact state, which tends to predict a deeper stress-affected region than that observed in practice. In addition, the model uses isotropic hardening and elastic unloading and does not consider the Bauschinger effect; therefore, it cannot fully reflect cycle-dependent material behavior.

Although quantitative discrepancies exist in the deeper region, the model still provides good predictions of near-surface residual stress, as well as the magnitude and position of the maximum compressive residual stress in terms of absolute value. It also correctly reproduces the trend of residual stress distribution along the depth direction. Therefore, the model can be effectively used for trend analysis and for evaluating the effects of process parameters during USRP. Accordingly, the model is particularly suitable for assessing trends in the near-surface region, which is important for the fatigue strength of components.

5. Conclusions

This study developed an analytical model based on Hertzian contact mechanics combined with an elastic–plastic mapping rule and unloading simulation to predict the depthwise distribution of compressive residual stress and the compressive layer depth of AA6061 aluminum alloy during the Ultrasonic Surface Rolling Process (USRP). Based on the investigation of four process parameters, including static force F_s, vibration amplitude A_0, ultrasonic frequency f, and rolling ball radius R_1, the main conclusions can be drawn as follows:

(1) The static force F_s has the most prominent influence on the depthwise distribution of compressive residual stress. As F_s increases within the investigated range, the compressive residual stress increases in absolute magnitude, and the position where the stress returns to the equilibrium state shifts deeper into the material, indicating an increasing trend in compressive layer depth.

(2) Both the vibration amplitude A_0 and ultrasonic frequency f increase the level of compressive residual stress and the compressive layer depth within the investigated range. Compared with the static force, the degrees of change caused by these two parameters are smaller, mainly reflected in the enhancement of compressive residual stress in the near-surface region and a slight shift in the compressive layer depth.

(3) The rolling ball radius R_1 exhibits a different influence mechanism compared with the other parameters. As R_1 increases, the maximum compressive residual stress in the near-surface region tends to decrease in absolute magnitude, whereas the compressive layer depth increases. This result indicates that a larger ball radius expands the depthwise affected region rather than increasing the surface compression level.

(4) Comparison with experimental data shows that the model correctly reproduces the trend of residual stress distribution along the depth direction, including the position of the maximum subsurface compressive region and the gradual decreasing trend with increasing depth into the material. Although quantitative discrepancies remain in the deeper region, the model is still suitable for trend analysis and qualitative evaluation of the effects of process parameters during USRP.

Acknowledgements: This work was supported by the Ho Chi Minh City University of Industry and Trade under the university-level science and technology project "Optimization of Process Parameters in Ultrasonic Surface Rolling of AA6061 Aluminum Alloy" (Research Contract No. 24/HĐ-ĐCT). The authors gratefully acknowledge the research facilities provided by the University.

REFERENCES

[1] X. Ma *et al.*, "Surface Properties and Fatigue Behavior of 6061 Aluminum Alloy by Multi-pass Ultrasonic Surface Rolling Process," *Journal of Materials Engineering and Performance,* vol. 34, no. 7, pp. 6159-6174, 2025.

[2] L. Li, M. Kim, S. Lee, J. Kim, H. Kim, and D. Lee, "Study on surface modification of aluminum 6061 by multiple ultrasonic impact treatments," *The International Journal of Advanced Manufacturing Technology,* vol. 96, no. 1, pp. 1255-1264, 2018.

[3] R. Teimouri, S. Amini, and A. B. Bami, "Evaluation of optimized surface properties and residual stress in ultrasonic assisted ball burnishing of AA6061-T6," *Measurement,* vol. 116, pp. 129-139, 2018.

[4] Z. Liu, C. Zhang, H. Zhao, V. Ji, and D. Wang, "Theoretical analysis and performance prediction on modified surface layer caused by ultrasonic surface rolling," *The International Journal of Advanced Manufacturing Technology,* vol. 113, no. 5, pp. 1307-1330, 2021.

[5] X. Ma *et al.*, "Effect of ultrasonic surface rolling process on surface properties and microstructure of 6061 aluminum alloy," *Materials Research,* vol. 26, p. e20230322, 2023.

[6] Y. Cheng, Y. Wang, Z. Wang, P. Huang, P. Zhang, and Q. Guo, "Ultrasonic surface rolling strengthening and its parameter optimization on bearing raceway," *Materials & Design,* vol. 232, p. 112156, 2023.

[7] X. Xue, S. Xu, Y. Pan, W. Zheng, J. Han, and J. Li, "Finite element analysis and surface performance study of high-speed precision bearing ultrasonic surface rolling processing," *Journal of Materials Engineering and Performance,* vol. 33, no. 21, pp. 11924-11936, 2024.

[8] J. Zheng, L. Jia, Y. Shang, H. Deng, and J. Li, "7075 aluminum alloy induced by ultrasonic surface rolling: grain refinement and residual stress model analysis and evaluation," *The International Journal of Advanced Manufacturing Technology,* vol. 131, no. 5, pp. 2823-2836, 2024.

[9] J. Zheng, Y. Shang, Y. Guo, H. Deng, and L. Jia, "Analytical model of residual stress in ultrasonic rolling of 7075 aluminum alloy," *Journal of Manufacturing Processes,* vol. 80, pp. 132-140, 2022.

[10] H. Liu, J. Zheng, Y. Guo, and L. Zhu, "Residual stresses in high-speed two-dimensional ultrasonic rolling 7050 aluminum alloy with thermal-mechanical coupling," *International Journal of Mechanical Sciences,* vol. 186, p. 105824, 2020.

[11] Z. Meng, Z. Yuanxi, and Z. Yang, "Theoretical and experimental analysis of compressive residual stress field on 6061 aluminum alloy after ultrasonic surface rolling process," *Proceedings of the Institution of Mechanical Engineers, Part C: Journal of Mechanical Engineering Science,* vol. 233, no. 15, pp. 5363-5376, 2019.

[12] M. Zhang, J. Deng, Z. Liu, and Y. Zhou, "Investigation into contributions of static and dynamic loads to compressive residual stress fields caused by ultrasonic surface rolling," *International Journal of Mechanical Sciences,* vol. 163, p. 105144, 2019.

[13] M. Zhang, Z. Liu, J. Deng, M. Yang, Q. Dai, and T. Zhang, "Optimum design of compressive residual stress field caused by ultrasonic surface rolling with a mathematical model," *Applied Mathematical Modelling,* vol. 76, pp. 800-831, 2019.

[14] K. L. Johnson, *Contact mechanics*. Cambridge university press, 1987.

[15] M. Sadd, "*Elasticity Theory, Applications, and Numerics, 4th*," Katey Birtcher, 2021.

[16] R. Abeyaratne, "*Lecture Notes on The Mechanics of Elastic Solids Volume II: Continuum Mechanics*," Lect. Notes II, p. 428, 2012.

[17] J. Li, Y. Mei, W. Duo, and W. Renzhi, "Mechanical approach to the residual stress field induced by shot peening," *Materials Science and Engineering: A,* vol. 147, no. 2, pp. 167-173, 1991.